

The SDSS-HET Survey of *Kepler* Eclipsing Binaries. A Sample of Four Benchmark Binaries.

KELLY HAMBLETON,¹ ANDREJ PRŠA,¹ SCOTT W. FLEMING,² SUVRATH MAHADEVAN,^{3,4} AND CHAD F. BENDER⁵

¹*Department of Astronomy & Astrophysics, Villanova University, 800 East Lancaster Ave., Villanova, PA 18085*

²*Space Telescope Science Institute, 3700 San Martin Dr, Baltimore, MD 21218*

³*Department of Astronomy & Astrophysics, The Pennsylvania State University, 525 Davey Lab, University Park, PA-16802*

⁴*Center for Exoplanets & Habitable Worlds, The Pennsylvania State University, 525 Davey Lab, University Park, PA-16802*

⁵*Department of Astronomy and Steward Observatory, University of Arizona, Tucson, AZ 85721*

ABSTRACT

The purpose of this work is to extend a sample of accurately modeled, benchmark-grade eclipsing binaries with accurately determined masses and radii. We select four “well-behaved” *Kepler* binaries, KIC 2306740, KIC 4076952, KIC 5193386 and KIC 5288543, each with at least 8 double-lined spectra from the APOGEE instrument that is part of the Sloan Digital Sky Surveys III and IV, and from the Hobby-Eberly High Resolution Spectrograph. We obtain masses and radii with uncertainties of 2.5% or less for all four systems. Three of these systems have orbital periods longer than 9 days, and thus populate an under-sampled region of the parameter space for extremely well-characterized detached eclipsing binaries. We compare the derived masses and radii against MESA MIST isochrones to determine the ages of the systems. All systems were found to be coeval, showing that the results are consistent across MESA MIST and PHOEBE.

Keywords: techniques: radial velocities — techniques: spectroscopic — techniques: photometric — binaries: eclipsing — stars: fundamental parameters

1. INTRODUCTION

To derive accurate stellar masses and radii, systems with strong constraints are required. When considering multiple star systems, the optimal case is a system of three or more stars where every component is eclipsing, cf. Carter et al. (2011b), as this places stringent constraints on the system geometry. However, these objects are rare and the software required to accurately model all time-dependent aspects of these systems within a Roche framework is still under construction (Conroy 2020). Another way to obtain accurate parameters is to look for totally eclipsing binaries (EBs) as the constraints for those cases, while not as stringent as for triples, provide us with better handles than partially eclipsing EBs. The goal of this work is to expand the library of accurate masses and radii upon which stellar evolutionary models can be validated.

Of course, alongside each well-behaved totally-eclipsing binary system, precise data are required to obtain the parameter accuracy goals. The *Kepler* satellite (Borucki et al. 2010) has provided a treasure trove of objects with highly precise data, which include 2922 binary stars (Prša et al. 2011; Slawson et al. 2011; Kirk et al. 2016). The level of detail obtained by the *Kepler* satellite has enabled approximate mass estimates to be extracted from *Kepler* light curves without the need for radial velocities through modeling ellipsoidal variations and Doppler boosting (see e.g. Carter et al. 2011a). This method offers the possibility of obtaining masses for objects that are not good candidates for radial velocity followup to a precision of $\sim 10\%$. For the purposes of calibrating stellar evolutionary models, however, we require masses and radii to a precision of $\leq 3\%$ (Morales et al. 2010) and aim for $\leq 2\%$. For this reason this work is based on a selection of four well-behaved eclipsing binary stars with a significant number of well-sampled radial velocity data points.

For the definition of well-behaved or benchmark-grade binary systems, we adopt the criteria of Torres et al. (2010), based on that of Andersen (1991), which states: the stellar components must appear to have evolved as if they were

single stars, which excludes any mass transfer; the spectra must be of high resolution and signal-to-noise; the period should be easily determined, *i.e.* there is no measurable apsidal motion; and the eclipses must both be significant such that the ratio of the temperatures can be determined through direct measurement (it is worthy of note that the absolute temperature of one of the components, though spectral fitting or similar, is necessary to remove degeneracies from the model). With these stringent requirements, we are able to provide a discriminating test of theoretical evolution models (Southworth et al. 2004). A catalog of established benchmark-grade eclipsing binaries that are subject to these criteria can be found in the DEBCat Library¹ (Southworth 2014).

This paper is the third in a series of papers describing objects from the *SDSS-HET Survey of Kepler EBs* (Bender et al. 2012; Mahadevan et al. 2019), which focus on the *Kepler* data and radial velocity data from the Sloan Digital Sky Survey (SDSS) and the Hobby-Eberly Telescope (HET). Throughout this paper, we will refer to details described in the original paper, Mahadevan et al. (2019), hereafter M19. Other works that have taken advantage of the overlap between APOGEE and *Kepler* to determine precise solutions for eclipsing binaries include Mahadevan et al. (2019), Cunningham et al. (2019) and Gaulme et al. (2016). The purpose of this paper is to provide benchmark-quality binary star models of four objects where the derived masses and radii are precise to better than 2.5% or better.

In Section 2 we describe the facilities and data products used for this work. In Section 3 we discuss the detailed analysis of the data, including Markov chain Monte Carlo methods and Gaussian process application for the noise model. In Section 4 we describe the four benchmark-grade binary stars that have been analysed, and in Section 5 we summarize the outlined work and provide concluding remarks.

2. FACILITIES AND DATASETS

2.1. *The Kepler Mission*

The *Kepler* satellite (Borucki et al. 2010), launched in 2009, simultaneously and continuously observed $\sim 156,000$ stars for ~ 4 yr. The telescope had a 0.95 m primary mirror and a high-precision white-light photometer with 42 CCDs. During its primary mission it monitored a 115 square-degree region of the sky in the direction of Cygnus and Lyra in an Earth trailing, heliocentric orbit. The nearly continuous observations generated unprecedented light curves that paved the way for numerous scientific advances in planetary science - the primary mission objective - but also for auxiliary goals such as binary star science.

For the purpose of this work we used *Kepler* long cadence observations (~ 30 min exposure time), which were downloaded from MAST (Mikulski Archive for Space Telescope). We elected to use the simple aperture photometry, which has been minimally processed by the *Kepler* pipeline. Prior to performing binary star analysis, we detrended and normalized the light curves by fitting a low order (order = 1–4) Legendre polynomial to each segment of data between breaks. Obvious outliers were additionally removed by eye.

As the *Kepler* light curve uncertainties are known to be underestimated (Bryson et al. 2011), we independently determined the uncertainties for each object by finding the standard deviation of multiple segments of the light curve. To do this, each out-of-eclipse segment was detrended by applying a high order (order = 3–20) polynomial. We aggressively detrended the lightcurve to remove all instrumental systematics and deviations due to spots and other astrophysical processes for the purpose of error estimation only. For each object, we took the median average of the standard deviation for 10 segments to determine the final uncertainty. To ensure the uncertainties were properly estimated, we additionally included a Gaussian noise term in our fitting procedure, which is discussed in detail in §3.5.

2.2. *The SDSS-III APOGEE Spectrometer*

The Apache Point Observatory Galactic Evolution Experiment (APOGEE, Majewski et al. 2017) is a fiber-fed, multi-object spectrometer on the 2.5 m telescope of the Sloan Digital Sky Survey (SDSS York et al. 2000; Gunn et al. 2006) located at Apache Point Observatory. It is a near-infrared instrument with a wavelength range of 1.51 to 1.68 μm and a resolution of $\lambda/\Delta\lambda \sim 22,500$. APOGEE can simultaneously observe 300 objects over a 3 deg diameter field of view.

The spectra discussed herein were observed during 2011 and became publicly available with Data Release 10 (Ahn et al. 2014). We start with the “apVisit” spectra produced by the SDSS pipeline, which are combined exposures that typically amount to a little over one hour of total observation time. We performed additional post-processing prior to generating radial velocities. We applied a low order polynomial to remove continuum and normalize each

¹ <http://www.astro.keele.ac.uk/jkt/debcats/>

spectrum. We additionally corrected for the imperfect correction of telluric absorption lines by manually interpolating over neighboring pixels. For additional details, we refer the reader to M19.

2.3. The HET High-Resolution Spectrograph

To complement the APOGEE spectroscopic data, we obtained optical spectra from the High-Resolution Spectrograph (hereafter HRS) on the Hobby-Eberly Telescope located on the McDonald Observatory. HRS is a visible-light, fiber-fed, cross-dispersed echelle spectrometer with a wavelength range of 4076 to 7838 Å and a resolution of $\lambda/\Delta\lambda \sim 30,000$.

Calibrations, including biases, flats and ThAr wavelength references, were obtained at the end of each night and additionally either before or after each observation. The HRS spectra were then channeled through a semi-automated pipeline which applies image processing, spectral extraction and wavelength calibration. As with the APOGEE spectra, continuum normalizing was performed as part of post-processing. We selected segments of the spectra that contain telluric contamination of 0.5% or less. Eight segments of spectra were used as part of our analysis: 4390–5025 Å, 5100–5410 Å, 5475–5680 Å, 5770–5855 Å, 6020–6260 Å, 6365–6430 Å, 6620–6850 Å and 7450–7580 Å. The spectra in our sample were observed between 2011 and 2013. Additional information regarding the HET reduction and pipeline can be found in the Appendix within M19.

3. ANALYSIS TECHNIQUES

3.1. Measurement of Radial Velocities

A requirement for our sample of benchmark-grade binary systems was that the spectra contained signatures of both stellar components. With both stars visible in the spectra, the mass ratio and the size of the orbit can be determined, which is imperative for obtaining accurate masses and radii.

To obtain radial velocities from the observed spectra, we applied our SXCORR implementation of TODCOR (Two Dimensional Cross Correlation, Zucker et al. 2003), which allows for segments of a spectrum with variable lengths. Previous works contain extensive descriptions of SXCORR, *i.e.* Bender & Simon (2008); Bender et al. (2012); Lockwood et al. (2014) and we refer the interested reader to the descriptions therein.

For the APOGEE spectra, we used synthetic templates generated from the PHOENIX-based BT-Settl model grid (Allard et al. 2011). The templates used for the HRS spectra consist of observations of early F through mid M dwarfs that were observed concurrently with the HRS EB observations, and additionally BT-Settl templates to ensure the full range of T_{eff} , $[M/H]$ and $\log g$ is covered. To generate a template from the BT-Settl library, we convolved the raw synthetic spectrum to the proper resolution (22,500 for APOGEE and 30,000 for HRS) and re-sampled to three pixels per resolution element. We additionally applied rotational broadening kernels based on the appropriate stellar parameters (Gray 1999; Claret et al. 2012). See Table 1 for the radial velocity measurements.

3.2. Binary Star Modeling

For each binary star in our sample we simultaneously modeled the *Kepler* lightcurve, and APOGEE and HRS radial velocity curves to determine accurate binary star parameters. To do this we used a combination of software: the binary star modeling software, PHOEBE 1.0 (Prša & Zwitter 2005), which is based on the Wilson-Devinney code (Wilson & Devinney 1971, hereafter WD); EMCEE, a PYTHON implementation of the affine invariant Markov chain Monte Carlo sampler proposed by Goodman & Weare (2010) and implemented by Foreman-Mackey et al. (2013); CELERITE (Foreman-Mackey et al. 2017), the Gaussian process library (Foreman-Mackey et al. 2017); and our own codes. We briefly describe the analysis here, but refer the reader to M19 for a more detailed description.

3.3. The PHOEBE Model

The PHOEBE modelling software combines the complete treatment of the Roche potential with the detailed treatment of surface and horizon effects such as limb darkening, reflection and gravity darkening to derive an accurate model of the binary system. PHOEBE uses the WD method of summing over the stellar surface using discrete trapezoidal elements to determine the total observed flux and consequently a complete set of stellar parameters. Additional to the standard functionality of WD, PHOEBE offers features including an intuitive graphical user interface, updated filters, and interfacing between PHOEBE and PYTHON.

As PHOEBE is computationally expensive when used within a Bayesian framework, we elected to compute the PHOEBE model in phase space, which significantly reduced the number of data points and thus computational time. This is appropriate as the selected binary systems do not present any temporal variations on timescales longer than that

Table 1. HRS & APOGEE RV Measurements.

UT Date	BJD-2,400,000	V_A (km s ⁻¹)	V_B (km s ⁻¹)	Instrument
<i>KIC 2306740</i>				
2011 Jul 21	55763.657622	-47.095±0.098	85.573±0.188	HRS
2011 Aug 24	55797.798841	80.442±0.094	-58.287±0.174	HRS
2011 Aug 28	55801.772678	6.212±0.098	25.530±0.194	HRS
2011 Oct 06	55840.667652	57.174±0.100	-32.382±0.188	HRS
2011 Oct 10	55844.647447	-27.296±0.114	63.953±0.210	HRS
2011 Oct 26	55860.612849	70.338±0.244	-47.579±0.460	HRS
2011 Sep 07	55811.613101	14.143±0.533	14.403±0.847	APG
2011 Oct 06	55840.593371	58.339±0.468	-34.714±0.747	APG
2011 Oct 17	55851.578556	43.858±0.476	-19.668±0.849	APG
<i>KIC 4076952</i>				
2011 Sep 01	2455805.79105	35.382±0.500	-4.510±0.375	HRS
2011 Sep 02	2455806.801811	-6.201±0.605	52.138±0.407	HRS
2011 Sep 14	2455818.757964	-39.184±0.988	97.335±0.884	HRS
2011 Sep 29	2455833.72453	76.907±0.48	-60.358±0.372	HRS
2011 Oct 24	2455858.639961	-24.586±0.64	75.868±0.360	HRS
2011 Nov 16	2455881.586275	79.316±0.307	-64.242±0.428	HRS
2011 Sep 19	2455823.72736952	79.902±0.336	-63.767±1.268	APG
2011 Oct 17	2455851.6496057	67.395±1.16	-47.523±3.203	APG
<i>KIC 5193386</i>				
2011 May 09	2455690.841836	7.638±0.98	-97.698±0.392	HRS
2011 Jun 24	2455736.715402	-9.475±0.28	-76.520±0.490	HRS
2011 Jul 06	2455748.705552	-54.475±0.86	-21.673±0.332	HRS
2011 Jul 19	2455761.661753	-55.979±0.42	-20.181±0.360	HRS
2011 Aug 19	2455792.795279	-35.731±0.400	-	HRS
2011 Aug 28	2455801.787839	-20.266±0.56	-62.673±0.318	HRS
2011 Sep 09	2455813.703058	-43.735±0.734	-	APG
2011 Sep 19	2455823.727087	-29.297±0.713	-	APG
2011 Oct 06	2455840.661733	7.215±0.586	-	APG
2011 Oct 15	2455849.578958	-81.657±0.855	10.365±2.620	APG
2011 Oct 17	2455851.649347	-87.364±0.998	13.654±2.999	APG
2011 Nov 01	2455866.569977	-30.531±0.914	-	APG
<i>KIC 5288543</i>				
2011 Sep 09	56151.614362	-45.535±0.210	129.722±0.417	HRS
2011 Sep 19	56154.83568	-49.213±0.204	133.655±0.405	HRS
2011 Oct 06	56204.697696	94.125±0.213	-55.371±0.424	HRS
2011 Oct 15	56209.679998	-15.013±0.204	89.170±0.378	HRS
2011 Oct 17	56213.690411	-49.740±0.343	135.083±0.527	HRS
2011 Nov 01	56262.546422	-21.577±0.299	97.404±0.368	HRS
2011 Sep 09	55813.703168	55.707±0.848	-	APG
2011 Sep 19	55823.727209	6.791±0.774	-	APG
2011 Oct 15	55849.579097	63.614±0.666	-	APG
2011 Oct 17	55851.649485	43.595±0.619	-	APG
2011 Nov 01	55866.570111	94.037±0.683	-	APG

of the orbit (with the exception of spots, which we model using Gaussian Processes in time space). Using PHOEBE, we simultaneously model the *Kepler* light curve, and APOGEE and HRS radial velocities. For each system we fit the following parameters: inclination i ; eccentricity e ; argument of periastron ω ; the primary and secondary surface potentials, Ω_1 and Ω_2 ; barycentric gamma velocity, γ ; the mass ratio q ; semi-major axis a ; third light l_3 ; and the effective temperature ratio $T_{\text{eff}2}/T_{\text{eff}1}$ (where the primary star temperature was fixed and the ratio of the temperatures was used as a fitted parameter due to its orthogonal nature). To ensure that our uncertainty estimates are accurate, we marginalize over the albedos, gravity darkening parameters and rotational velocities, $v \sin i$, for both components.

The selected limb darkening law primarily affects the fit at the ingress and egress portion of the eclipses, thus has implications for the determination of the radii. It is currently unclear which is the preferred limb-darkening law (Maxted et al. 2020), thus we applied the square root limb darkening law to our models, which has been shown by Diaz-Cordoves & Gimenez (1992) to work best for objects that radiate towards the IR.

3.4. Markov chain Monte Carlo Methods

We incorporated EMCEE, a Markov chain Monte Carlo (MCMC) sampler, to sample the parameters' posterior probability distributions within a Bayesian framework. The log-likelihood distribution function was calculated at each iteration:

$$\log P(\theta|D) = \log P(F|\theta) + \log P(RV|\theta) + \log P(GP|\theta) + \log P(\theta) + C, \quad (1)$$

where D denotes the data, F are the light curve measurements, RV are the radial velocity measurements, GP denotes the Gaussian process noise model, θ is the parameter vector that contains the fitted parameters (specified in §3.3) and C is an arbitrary constant. A significant benefit of MCMC is that the results are given as posterior probability distributions. By considering these distributions, and subsequently the joint parameter distributions, we are able to see how well the parameter values are determined with respect to the data set.

For each of the fitted parameters in §3.3 we started with an initial distribution which represents a tight N -dimensional cube around all parameters in phase space. For each parameter, we applied a uniform prior that encompassed all allowable configurations and additionally marginalized over $v \sin i$ for both components. To constrain our models, we elected to use 288 walkers during the initial burn in time, while the model was visibly converging, and 144 walkers for the remaining duration. We elected to use 288 and 144 walkers as the number of walkers can be equally divided between the available processors (72), which optimizes the time required per iteration (each processor generates 4 or 2 models per iteration, respectively). To estimate convergence, we required a minimum of ten auto-correlation timescales, as recommended by Foreman-Mackey et al. (2013), although in practice we typically acquired greater than 50.

3.5. Noise modeling using Gaussian Processes

We elected to model the systematic noise and unwanted astrophysical signals, such as spots, using the Gaussian Processes (GP) package CELERITE. A Gaussian process is a collection of random variables, any finite number of which have joint Gaussian distributions. Within our model the GPs were conditioned on the data so that they were distributed normally with respect to the data. Rather than fitting a function to the noise in our data, we applied GPs to determine the probability distribution over all possible functions that fit the noise. By fitting the high-level parameters of a covariance kernel, GPs enabled a better treatment of noise and poorly understood error correlations in the heteroscedastic data.

Once the model light and radial velocity curves had been created using PHOEBE and EMCEE, we applied GPs to the model light curve in time space. At the heart of GPs is the kernel or covariance function, which encodes our assumptions about the nearness or similarity between data points. For more information on covariance functions, we direct the interested reader to Chapter 4 of Rasmussen & Williams (2006). For our work we selected a term that is a Taylor-series expansion of the Matérn 3/2 kernel function. The Matérn 3/2 has rapidly and slowly varying components and thus is optimal for modeling long term trends such as spots and more rapid features such as instrumental variations:

$$k(\tau) = \sigma^2 \left[(1 + 1/\epsilon)e^{-(1-\epsilon)\sqrt{3}\tau/\rho} (1 + 1/\epsilon)e^{-(1+\epsilon)\sqrt{3}\tau/\rho} \right] \quad (2)$$

where σ and ρ are the only two tunable parameters and ϵ controls the quality of the approximation since, in the limit as $\epsilon \rightarrow 0$, Equation (2) becomes the Matérn-3/2 function.

In §2.1 we detailed the method used to determine the uncertainties in the light curve. As an additional measure, we applied the jitter kernel to our model to assess the designated uncertainties. The jitter kernel takes the form:

$$k(\tau_{n,m}) = \sigma^2 \delta_{n,m}, \quad (3)$$

where σ is a tunable parameter. In the case that our uncertainties are underestimated, the value of σ is significant with respect to the uncertainties and white noise is added to the model. We primarily apply the jitter kernel to assess the uncertainties determined in §2.1.

3.6. Comparison with Stellar Evolutionary Models

To verify our results, validate the stellar evolution models and to determine the age of each binary system, we generate isochrone models for each binary star and showed that, for each binary star analysed, both components lie on the same isochrone. We use the MIST (MESA Isochrones and Stellar Tracks) software (Dotter 2016; Choi et al. 2016), which is based on the MESA (Modules for Experiments in Stellar Astrophysics) package (Paxton et al. 2011, 2013, 2015). The models include time-dependent, diffusive, convective overshoot (Herwig 2000), Asplund et al. (2009) solar abundances and the OPAL (Iglesias & Rogers 1993, 1996) opacities. For each system we used the metallicity and primary star T_{eff} determined from APOGEE data release 16 (Jönsson et al. 2020). We are able to assume that the APOGEE temperatures are equivalent to the primary temperatures as all systems have a small H-band flux ratio, which infers that the contribution of the secondary component to the determined temperature is not substantial.

4. FUNDAMENTAL PARAMETERS FOR FOUR BENCHMARK-GRADE ECLIPSING BINARIES

For each binary star, the precise radial velocities and *Kepler* light curves have been modeled using PHOEBE, EMCEE and CELERITE. The results comprise accurate masses and radii for all components, shown in Table 2.

4.1. KIC 2306740

KIC 2306740 consists of two F-type stars in a binary system with a 10.30699 ± 0.00003 d orbital period. The system exhibits a periodic oscillation in the out of eclipse region, as seen in Figure 1. The amplitude and frequency of the oscillation are variable over long timescales (visible on the timescale of the dataset), making pulsations unlikely as the cause of the variation. The Fourier transform exhibits two significant peaks, the second (2.7280 d^{-1}) the harmonic of the first (1.36387 d^{-1}), indicative of spots (Lanza et al. 1994; Zhan et al. 2019). If that is indeed the case, one object is rotating 3.8 times per orbit, consistent with our findings for the secondary object (from the binary model) to be rotating at a rate of 2.8 ± 1.3 times per orbit.

The fundamental parameters of KIC 2306740 were determined to be: $M_A = 1.227 \pm 0.017 M_{\odot}$, $M_B = 1.085 \pm 0.012 M_{\odot}$, $R_A = 1.734 \pm 0.007 R_{\odot}$ and $R_B = 1.215 \pm 0.005 R_{\odot}$. The distributions of these parameters can be seen in Figure 2. The exceptionally low ($< 1.5\%$) uncertainties can be attributed to the combination of the precise *Kepler* light curve (see Figure 1) and the precise radial velocity measurements that sample the orbital phase very well (see Figure 3).

Even with the small uncertainties, the two components of KIC 2306740 land on the same isochrone (see Figure 4), which places the two stars at ~ 3.3 Gyr with a metallicity of $[\text{Fe}/\text{H}] = -0.59$, as determined by the DR16 catalog (-0.59 ± 0.02).

4.2. KIC 4076952

KIC 4076952 contains a mid A- and early F-type star in a 9.76116 ± 0.00002 d orbit. The out-of-eclipse variations seen in the light curve (Figure 5) can be attributed to ellipsoidal variations, which are appropriately fitted within PHOEBE’s Roche framework. The fundamental parameters, provided as distributions in Figure 6, were determined to be: $M_A = 1.86 \pm 0.03 M_{\odot}$, $M_B = 1.37 \pm 0.02 M_{\odot}$, $R_A = 3.078 \pm 0.016 R_{\odot}$ and $R_B = 1.451 \pm 0.008 R_{\odot}$. The parameters have been determined through a simultaneous fit to the light and radial velocity curves (see Figures 5 and 7, respectively).

The stellar isochrones, which were ascribed a metallicity of $[\text{Fe}/\text{H}] = -0.06$, suggest that the two stars are ~ 1.2 Gyr old and that the primary star is starting to evolve off the main sequence (shown by its proximity to the red line in Figure 8). The metallicity determined by the DR16 pipeline is $[\text{Fe}/\text{H}] = -0.06 \pm 0.04$.

Table 2. Model parameters for the four benchmark eclipsing binaries

Parameter	KIC 2306740	KIC 4076952	KIC 5193386	KIC 5288543
<i>DR16 APOGEE parameters</i>				
T_A (K)	5570±140	6590±220	4770±100	6280±170
[Fe/H]	-0.59±0.02	-0.06±0.04	-0.50±0.01	-0.55±0.03
<i>Derived Orbital Parameters</i>				
Period	10.30699±0.00003	9.76116±0.00002	21.37829±0.00009	3.457075±0.000006
T_0	54966.425±0.067	54966.703±0.073	54980.20±0.17	54964.805±0.032
i (deg)	88.809±0.003	88.915±0.002	88.921±0.002	88.183±0.0002
e	0.3072±0.004	0.0306±0.0001	0.0092±0.002	0.0030±0.0001
ω (rad)	4.7881±0.0001	0.958±0.003	0.8016±0.0015	3.86±0.04
Ω_A	16.56±0.01	10.007±0.007	10.67±0.01	8.52±0.01
Ω_B	20.69±0.14	15.64±0.04	29.0±0.4	11.34±0.09
l_3 (%)	0.02±0.025	0.033±0.001	0.007±0.004	0.002±0.002
K_A	63.76±0.29	62.6±0.3	47.49±0.33	78.85±0.43
K_B	72.14±0.44	84.8±0.5	57.1±0.7	104.14±0.61
γ	15.10±0.18	18.1±0.3	-40.04±0.23	29.6±0.3
q	0.884±0.006	0.738±0.002	0.831±0.011	0.757±0.007
a (R_\odot)	26.35±0.11	28.42±0.14	44.2±0.3	12.51±0.04
<i>Physical Parameters</i>				
M_A (M_\odot)	1.227±0.017	1.86±0.03	1.386±0.036	1.251±0.015
M_B (M_\odot)	1.085±0.012	1.37±0.02	1.152±0.020	0.947±0.010
R_A (R_\odot)	1.734±0.007	3.078±0.016	4.505±0.032	1.6208±0.0055
R_B (R_\odot)	1.215±0.005	1.451±0.008	1.319±0.009	0.9272±0.0032
T_B/T_A	0.9655±0.0004	1.0137±0.0003	1.3862±0.0011	0.8905±0.0001
$L_A/(L_A + L_B)$	0.70224±0.00033	0.81122±0.00022	0.7587±0.0005	0.83010±0.00008
<i>Gaussian Process Parameters</i>				
$\log(\phi_{\text{matern}})$	-1.493±0.011	-1.869±0.013	-1.67±0.02	-1.7±0.2
$\log(\rho_{\text{matern}})$	2.005±0.005	2.89±0.01	2.012±0.009	2.9±0.19
$\log(\phi_{\text{jitter}})$	-7.485±0.001	-8.973±0.005	-8.9397±0.0009	-7.899±0.003

4.3. KIC 5193386

KIC 5193386 is an eclipsing binary star in a 21.37829 ± 0.00009 d orbit with one evolved F-type star and one main sequence F-type star. The obvious spots in the light curve (as seen in Figure 9) are commonly found on red giant stars and thus are attributed to the evolved component. Within our model, spots are treated as astrophysical noise and thus we account for them using Gaussian processes.

From modeling the binary star light and radial velocity curves (as seen in Figures 9 and 10, respectively), we determined the fundamental parameters to be: $M_A = 1.386 \pm 0.036 M_\odot$, $M_B = 1.152 \pm 0.020 M_\odot$, $R_A = 4.505 \pm 0.032 R_\odot$ and $R_B = 1.319 \pm 0.009 R_\odot$, which are shown as distributions in Figure 11.

The stellar isochrones, as depicted in Figure 12, show lines of equal age for stars with a metallicity of $[\text{Fe}/\text{H}] = -0.5$ as determined through spectral template fitting, $[\text{Fe}/\text{H}] = -0.5 \pm 0.01$. Both stars lie on the 2.5 Gyr isochrone with the more massive star lying on the brown line, which is the red giant branch segment of the isochrone.

4.4. KIC 5288543

KIC 5288543 consists of two main sequence stars, an F-type and G-type star, in a 3.457075 ± 0.000006 d binary orbit. The out of eclipse variations in the light curve (see Figure 13) can be attributed a combination of ellipsoidal variations, which are fitted by PHOEBE, and spots, which are fitted by gaussian processes. The spots and ellipsoidal variations are easily separated as the spot signal varies significantly over the data set whereas the ellipsoidal variable signal does not.

The detailed binary light curve and radial velocity curves, as shown in Figures 13 and 14 are well sampled and consequently provide accurate fundamental stellar parameters: $M_A = 1.251 \pm 0.015 M_\odot$, $M_B = 0.947 \pm 0.010 M_\odot$, $R_A = 1.6208 \pm 0.0055 R_\odot$ and $R_B = 0.9272 \pm 0.0032 R_\odot$, which are depicted as distributions in Figure 15.

As seen in Figure 16, both stars land on the 2.5 Gyr stellar isochrone showing that the stars are coeval, as expected. The generated isochrones are evolutionary tracks for stars with metallicity $[\text{Fe}/\text{H}] = -0.55$, as determined for this system through the DR16 pipeline. The primary star is relatively close to the brown segment of the 2.5 Gyr isochrone, which denotes the star has almost evolved off the main sequence.

5. DISCUSSION AND CONCLUSIONS

We thoroughly characterized four benchmark-grade eclipsing binaries, with periods of $\sim 3.5, 9.7, 10.3,$ and 21 d, that have been observed by *Kepler*, APOGEE and HET. The identified targets were selected from the *Kepler* catalog due to their well behaved lightcurves and well sampled radial velocity curves. We further required a significant number (> 8) of well-distributed high-resolution double-lined spectra for the precise determination of stellar masses and the semi-major axis (which provides a scaling factor for the radii).

For each object we applied SXCORR, our own implementation of TODCOR, to extract radial velocities. We subsequently generated a binary star model of the light curve and radial velocity data simultaneously using PHOEBE, EMCEE and CELERITE. By incorporating Gaussian processes into the likelihood function, we were able to properly model the stochastic and systematic noise to produce accurate parameter values.

Finally, we plotted the derived masses and radii against stellar isochrones. This allowed us to validate our assumption of co-eval objects, determine the age of each system and the evolutionary state of each star. Through the use of the stellar isochrone models, we additionally determined that the primary component of KIC 4076952 and KIC 5288543 are close to evolving off the main sequence and that the primary component of KIC 5193386 is a red giant on the red giant branch. These results provide further validation for our semi-automated modeling pipeline through consistency with the MESA MIST isochrones.

Software: PYTHON (Van Rossum & Drake 2009), KEPHEM (Prša et al. 2011), PHOEBE (Prša & Zwitter 2005), EMCEE (Foreman-Mackey et al. 2013), CELERITE (Foreman-Mackey et al. 2017), ASTROPY (Astropy Collaboration et al. 2013; Price-Whelan et al. 2018)

6. ACKNOWLEDGEMENTS

The authors express their sincere thanks to NASA and the *Kepler* team for the amazing, high-quality *Kepler* data. The *Kepler* mission is funded by NASA’s Science Mission Directorate. KH acknowledges support through NASA ADAP grant 80NSSC19K0594. We further acknowledge support from the NSF (grant #1517592). The authors would additionally like to thank the anonymous referee for their helpful comments that improved this manuscript.

This work was based on observations with the SDSS 2.5-meter telescope. Funding for SDSS-III has been provided by the Alfred P. Sloan Foundation, the Participating Institutions, the National Science Foundation, and the U.S. Department of Energy of Science. The SDSS-III web site is <http://www.sdss3.org/>. SDSS-III is managed by the Astrophysical Research Consortium for the Participating Institutions of the SDSS-III Collaboration including the University of Arizona, the Brazilian Participation Group, Brookhaven National Laboratory, University of Cambridge, Carnegie Mellon University, University of Florida, the French Participation Group, the German Participation Group, Harvard University, the Instituto de Astrofísica de Canarias, the Michigan State/Notre Dame/JINA Participation Group, Johns Hopkins University, Lawrence Berkeley National Laboratory, Max Planck Institute for Astrophysics, Max Planck Institute for Extraterrestrial Physics, New Mexico State University, New York University, Ohio State University, Pennsylvania State University, University of Portsmouth, Princeton University, the Spanish Participation Group, University of Tokyo, University of Utah, Vanderbilt University, University of Virginia, University of Washington, and Yale University.

Data presented herein were also obtained at the Hobby Eberly Telescope (HET), a joint project of the University of Texas at Austin, the Pennsylvania State University, Stanford University, Ludwig-Maximilians- Universität München, and Georg-August-Universität Göttingen. The HET is named in honor of its principal benefactors, William P. Hobby and Robert E. Eberly.

REFERENCES

- Ahn, C. P., Alexandroff, R., Allende Prieto, C., et al. 2014, *ApJS*, 211, 17
- Allard, F., Homeier, D., & Freytag, B. 2011, *Astronomical Society of the Pacific Conference Series*, Vol. 448, *Model Atmospheres From Very Low Mass Stars to Brown Dwarfs*, ed. C. Johns-Krull, M. K. Browning, & A. A. West, 91

- Andersen, J. 1991, *A&AR*, 3, 91
- Asplund, M., Grevesse, N., Sauval, A. J., & Scott, P. 2009, *ARAA*, 47, 481
- Astropy Collaboration, Robitaille, T. P., Tollerud, E. J., et al. 2013, *A&A*, 558, A33
- Bender, C. F., & Simon, M. 2008, *ApJ*, 689, 416
- Bender, C. F., Mahadevan, S., Deshpande, R., et al. 2012, *ApJ*, 751, L31
- Borucki, W. J., Koch, D., Basri, G., et al. 2010, *Science*, 327, 977
- Bryson, S., Jenkins, J., Gilliland, R., et al. 2011, in *American Astronomical Society Meeting Abstracts*, Vol. 217, *American Astronomical Society Meeting Abstracts #217*, 140.05
- Carter, J. A., Rappaport, S., & Fabrycky, D. 2011a, *ApJ*, 728, 139
- Carter, J. A., Fabrycky, D. C., Ragozzine, D., et al. 2011b, *Science*, 331, 562
- Choi, J., Dotter, A., Conroy, C., et al. 2016, *ApJ*, 823, 102
- Claret, A., Hauschildt, P. H., & Witte, S. 2012, *VizieR Online Data Catalog*, J/A+A/546/A14
- Conroy, K. E. 2020, *Contributions of the Astronomical Observatory Skalnaté Pleso*, 50, 530
- Cunningham, J. M. C., Rawls, M. L., Windemuth, D., et al. 2019, in *American Astronomical Society Meeting Abstracts*, Vol. 233, *American Astronomical Society Meeting Abstracts #233*, 418.06
- Diaz-Cordoves, J., & Gimenez, A. 1992, *A&A*, 259, 227
- Dotter, A. 2016, *ApJS*, 222, 8
- Foreman-Mackey, D., Agol, E., Angus, R., & Ambikasaran, S. 2017, *ArXiv*
- Foreman-Mackey, D., Hogg, D. W., Lang, D., & Goodman, J. 2013, *PASP*, 125, 306
- Gaulme, P., McKeever, J., Jackiewicz, J., et al. 2016, *ApJ*, 832, 121
- Goodman, J., & Weare, J. 2010, *Com. App. Math. Comp. Sci.*, 5, 65
- Gray, R. O. 1999, *SPECTRUM: A stellar spectral synthesis program*, , ascl:9910.002
- Gunn, J. E., Siegmund, W. A., Mannery, E. J., et al. 2006, *AJ*, 131, 2332
- Herwig, F. 2000, *A&A*, 360, 952
- Iglesias, C. A., & Rogers, F. J. 1993, *ApJ*, 412, 752
- . 1996, *ApJ*, 464, 943
- Jönsson, H., Holtzman, J. A., Allende Prieto, C., et al. 2020, *AJ*, 160, 120
- Kirk, B., Conroy, K., Prša, A., et al. 2016, *AJ*, 151, 68
- Lanza, A. F., Rodono, M., & Zappala, R. A. 1994, *A&A*, 290, 861
- Lockwood, A. C., Johnson, J. A., Bender, C. F., et al. 2014, *ApJ*, 783, L29
- Mahadevan, S., Bender, C. F., Hambleton, K., et al. 2019, *ApJ*, 884, 126
- Majewski, S. R., Schiavon, R. P., Frinchaboy, P. M., et al. 2017, *AJ*, 154, 94
- Maxted, P. F. L., Gaulme, P., Graczyk, D., et al. 2020, *MNRAS*, 498, 332
- Morales, J. C., Gallardo, J., Ribas, I., et al. 2010, *Astronomical Society of the Pacific Conference Series*, Vol. 435, *Low-Mass Eclipsing Binaries as Constraints for Stellar Structure Models*, ed. A. Prša & M. Zejda, 141
- Paxton, B., Bildsten, L., Dotter, A., et al. 2011, *ApJS*, 192, 3
- Paxton, B., Cantiello, M., Arras, P., et al. 2013, *ApJS*, 208, 4
- Paxton, B., Marchant, P., Schwab, J., et al. 2015, *ApJS*, 220, 15
- Price-Whelan, A. M., Sipőcz, B. M., Günther, H. M., et al. 2018, *AJ*, 156, 123
- Prša, A., & Zwitter, T. 2005, *ApJ*, 628, 426
- Prša, A., Batalha, N., Slawson, R. W., et al. 2011, *AJ*, 141, 83
- Rasmussen, C. E., & Williams, C. K. I. 2006, *Gaussian Processes for Machine Learning*
- Slawson, R. W., Prša, A., Welsh, W. F., et al. 2011, *AJ*, 142, 160
- Southworth, J. 2014, *The DEBCat detached eclipsing binary catalogue*, , arXiv:1411.1219
- Southworth, J., Maxted, P. F. L., & Smalley, B. 2004, *MNRAS*, 349, 547
- Torres, G., Andersen, J., & Giménez, A. 2010, *A&AR*, 18, 67
- Van Rossum, G., & Drake, F. L. 2009, *Python 3 Reference Manual* (Scotts Valley, CA: CreateSpace)
- Wilson, R. E., & Devinney, E. J. 1971, *ApJ*, 166, 605
- York, D. G., Adelman, J., Anderson, John E., J., et al. 2000, *AJ*, 120, 1579
- Zhan, Z., Günther, M. N., Rappaport, S., et al. 2019, *ApJ*, 876, 127
- Zucker, S., Mazeh, T., Santos, N. C., Udry, S., & Mayor, M. 2003, *A&A*, 404, 775

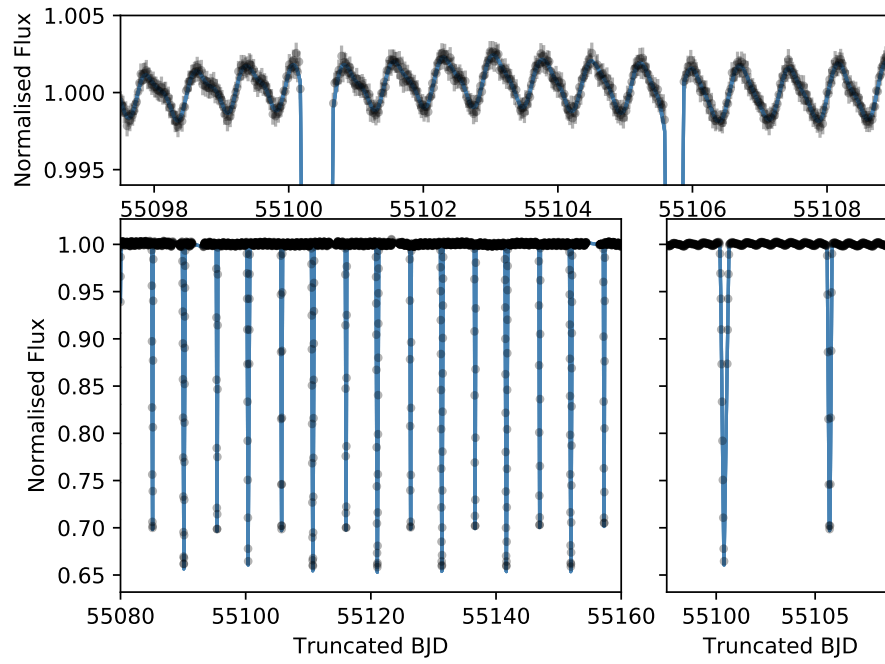


Figure 1. The *Kepler* light curve of KIC 2306740. Here the black points denote the *Kepler* data and the blue lines denote the PHOEBE binary star model and Gaussian processes combined. The out of eclipse variation has been attributed to spots.

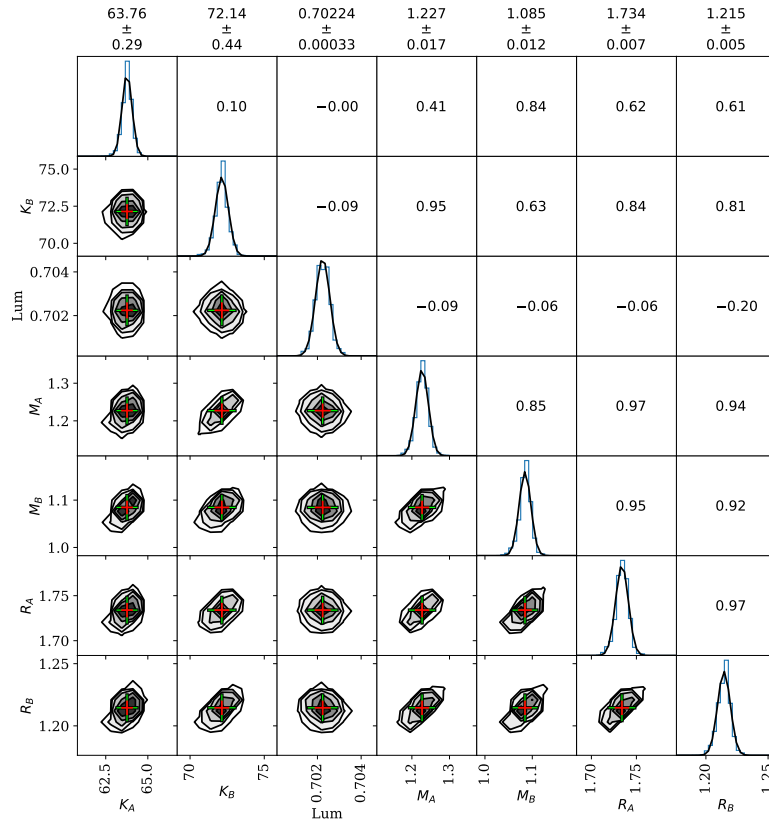


Figure 2. Distributions for the calculated parameters of KIC 2306740 where K is the semi-amplitude, Lum is the Luminosity ratio ($L_A/(L_A + L_B)$), and M and R are the Mass and Radius, respectively. The lower left section shows the 2-D parameter cross sections and the values reflected about the diagonal are the correlation parameter associated with each cross section. The histograms on the diagonal represent the distributions for each individual parameter and the values across the top are the mean and standard deviation based on the Gaussian fit to the histograms.

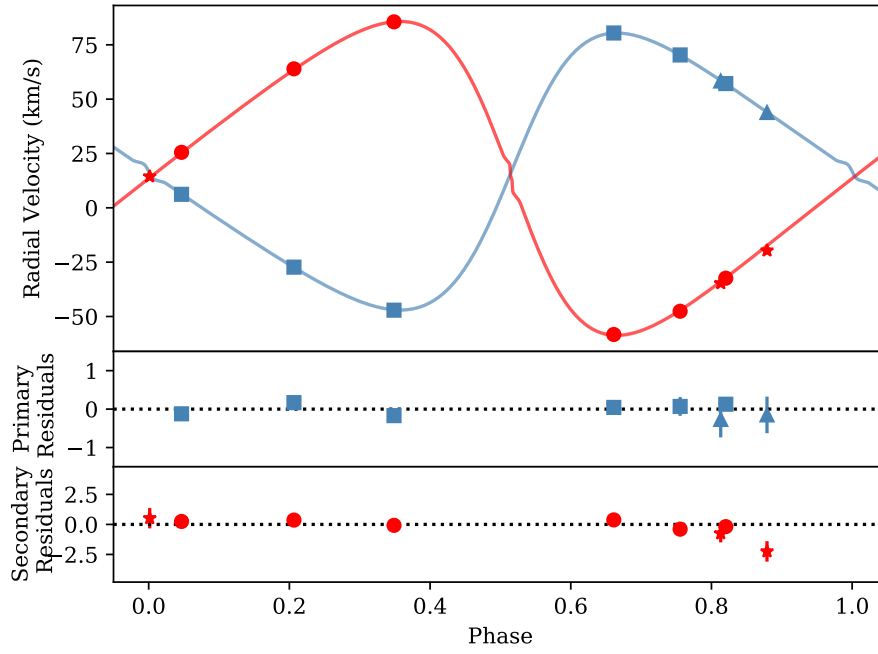


Figure 3. The figure shows the APOGEE and HRS radial velocities for KIC 2306740. Here the HRS radial velocities are denoted by blue squares (primary) and red circles (secondary), and APOGEE observations are denoted by the blue triangles (primary) and red stars (secondary). The blue and red lines denote the PHOEBE model for the primary and secondary components, respectively. The lower panels depict the residuals for the primary and secondary components. Note the Rossiter-McLaughlin effect is visible for both stars as they are eclipsed.

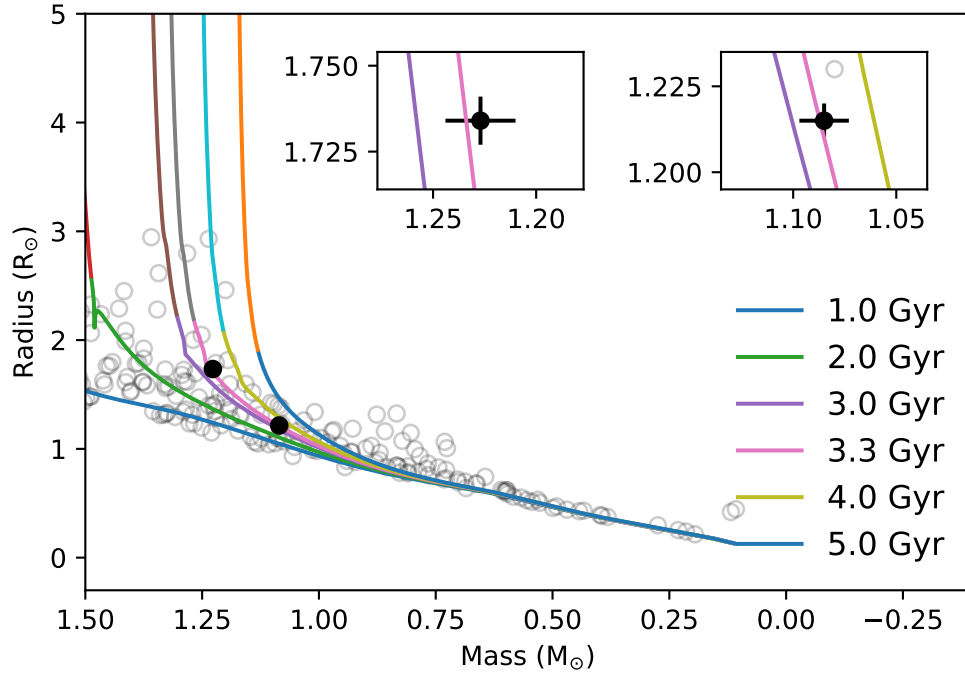


Figure 4. Radius versus mass, plotted for the EBs in the DEBCat Eclipsing Binary Catalog (open circles), an updated version of the Andersen (1991) catalog, along with the two components of KIC 2306740 (solid black circles). For comparison, we show MIST (MESA Isochrones and Stellar Tracks) stellar isochrones (Dotter 2016; Choi et al. 2016). The inserts depict magnified regions for the primary and secondary components.

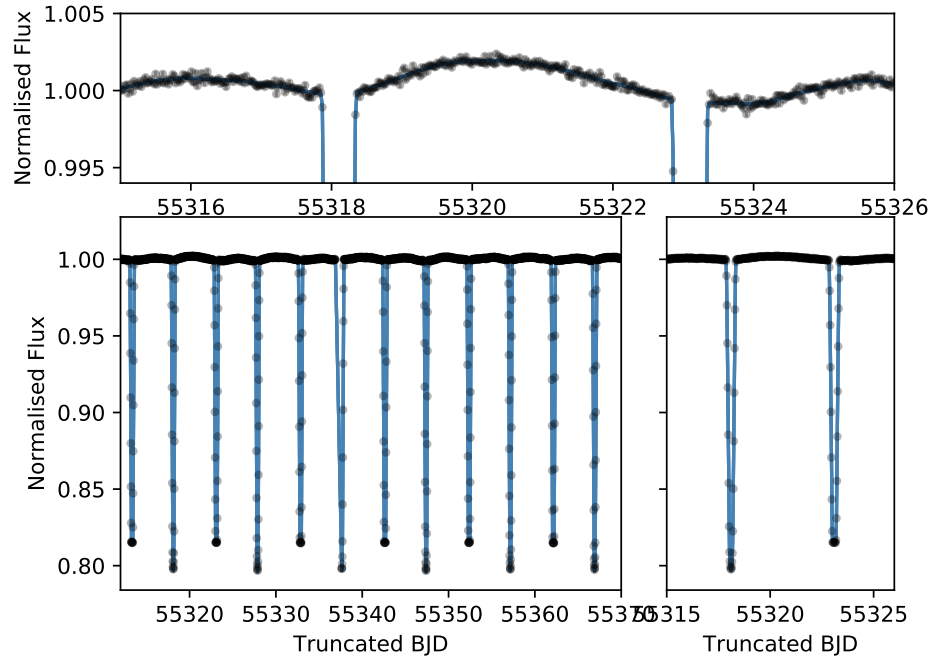


Figure 5. The *Kepler* light curve of KIC 4076952. Here the *Kepler* data are displayed as black points and the blue lines denote the PHOEBE binary star model and Gaussian processes combined.

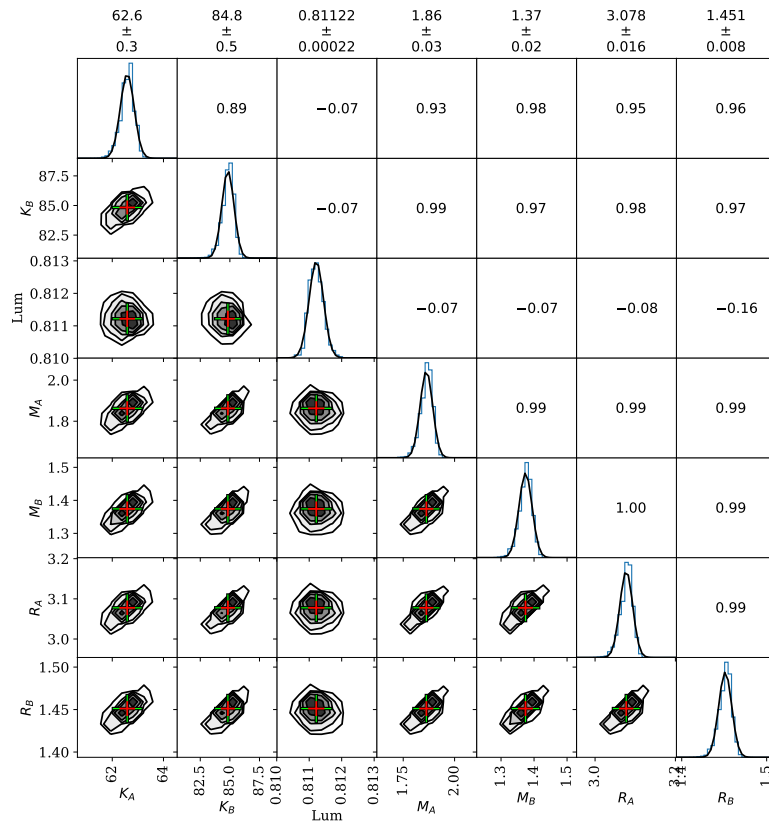


Figure 6. Distributions for KIC 4076952 where the figure has the same format as Figure 2

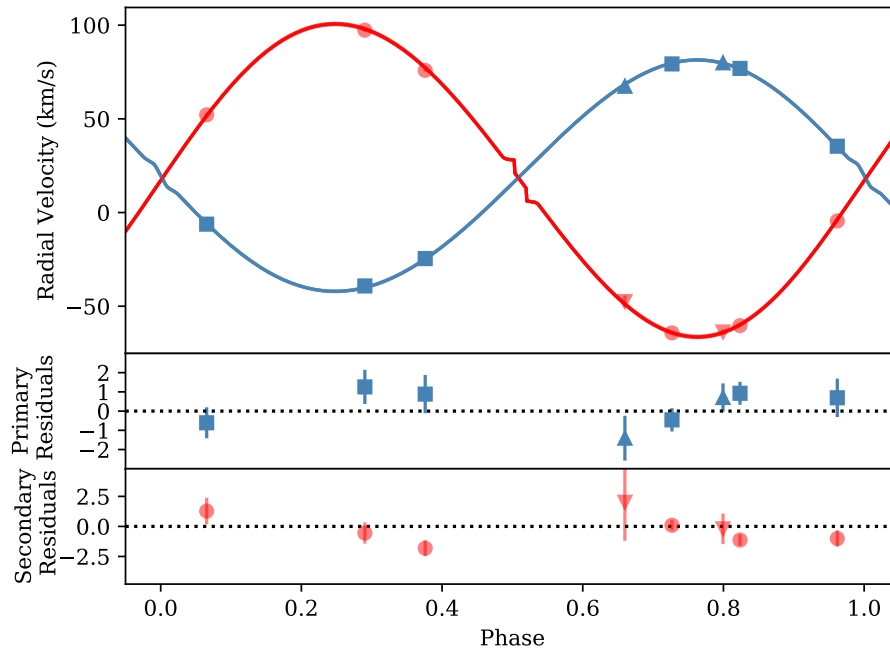


Figure 7. The figure depicts the APOGEE and HRS radial velocities, and PHOEBE model radial velocity curves for KIC 4076952. The residuals show significant scatter with respect to the derived TODCOR uncertainties, we attribute this to the uncertainties being slightly underestimated. The format is the same as that of Figure 3.

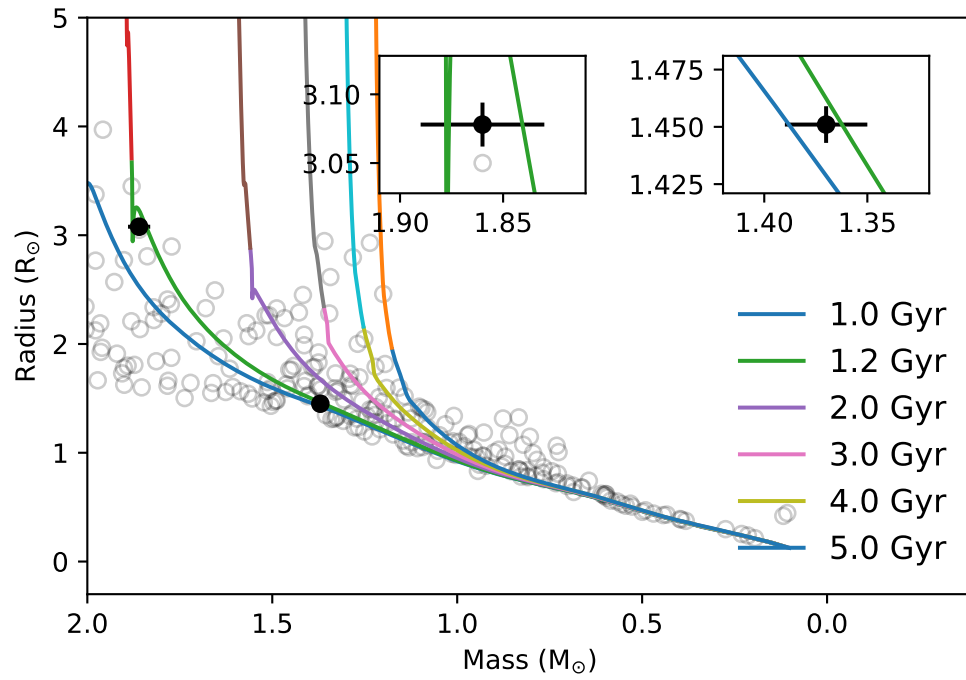


Figure 8. Radius vs mass for the components of KIC 4076952 where the figure is the same as Figure 4.

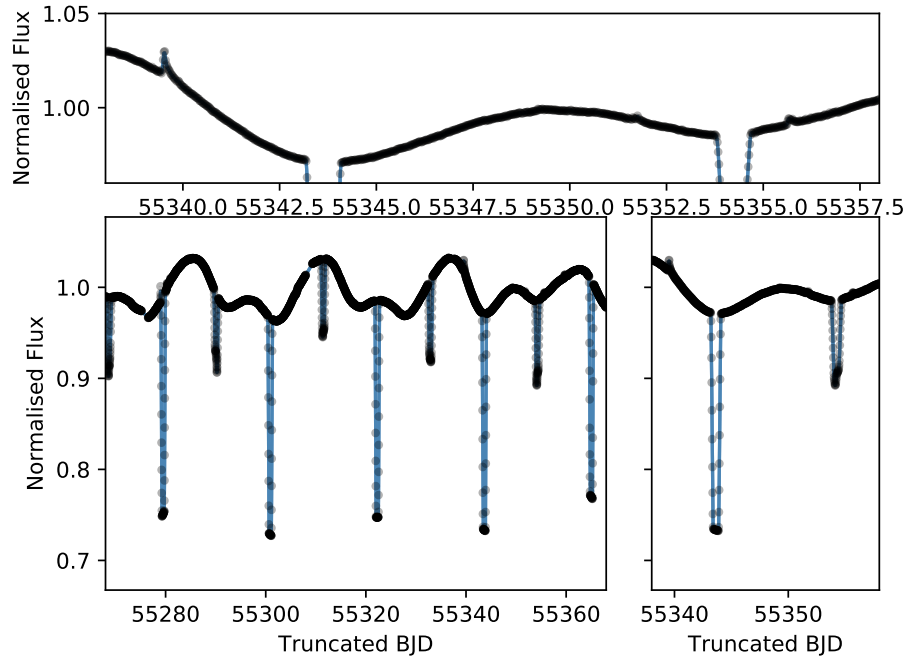


Figure 9. The *Kepler* light curve of KIC 5193896. Here the *Kepler* data are displayed as black points and the blue lines denote the PHOEBE binary star model and Gaussian processes combined. The significant variation in the envelope of the light curve are due to spots on the primary red giant component.

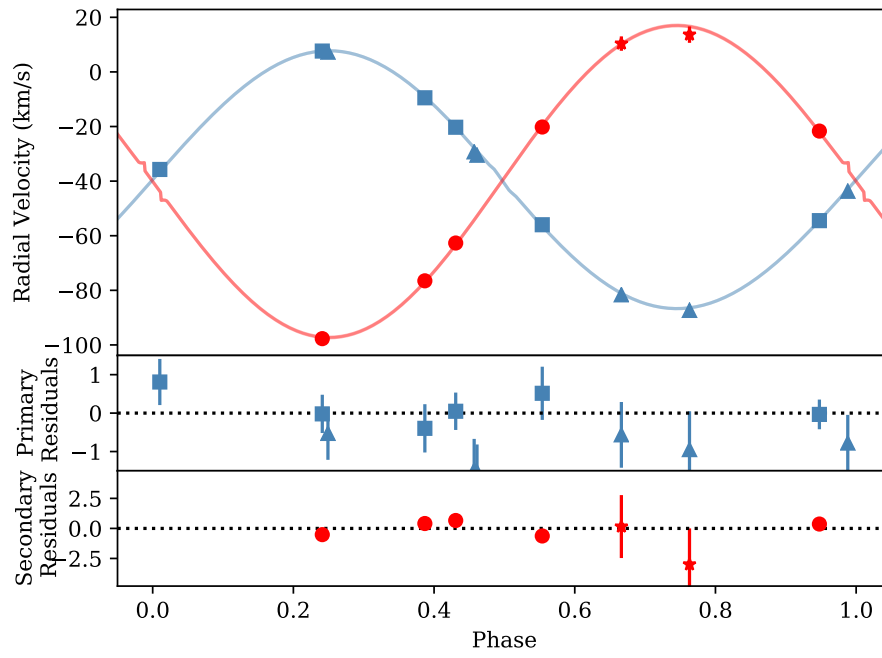


Figure 10. The figure depicts the APOGEE and HRS radial velocities, and PHOEBE model radial velocity curves for KIC 5193386. The format is the same as that of Figure 3.

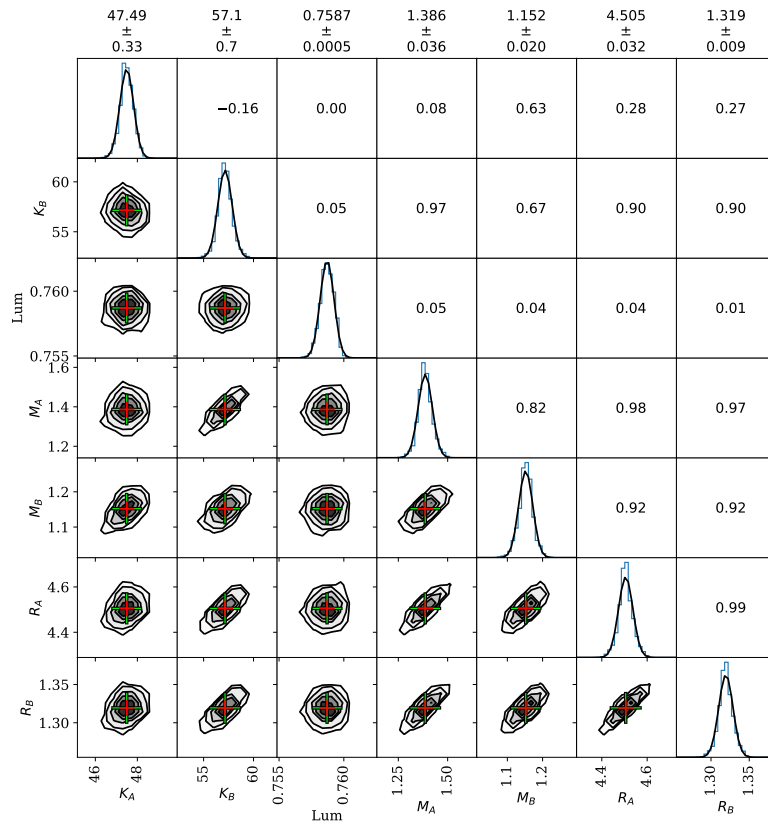


Figure 11. Distributions for KIC 5193386 where the figure has the same format as Figure 2.

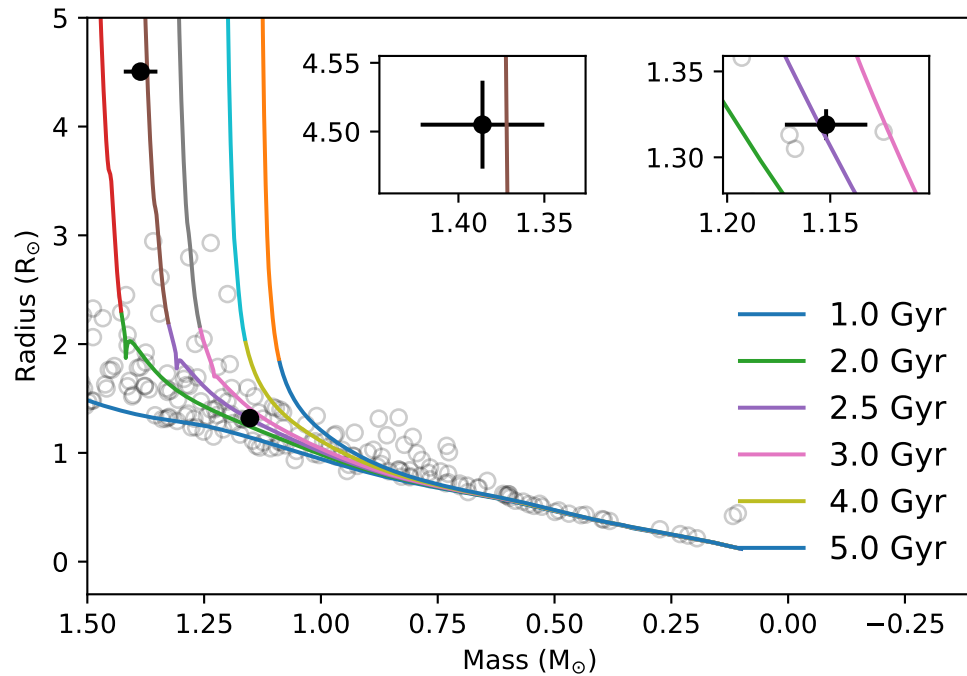


Figure 12. Radius vs mass for the components of KIC 5193386 where the figure is the same as Figure 4.

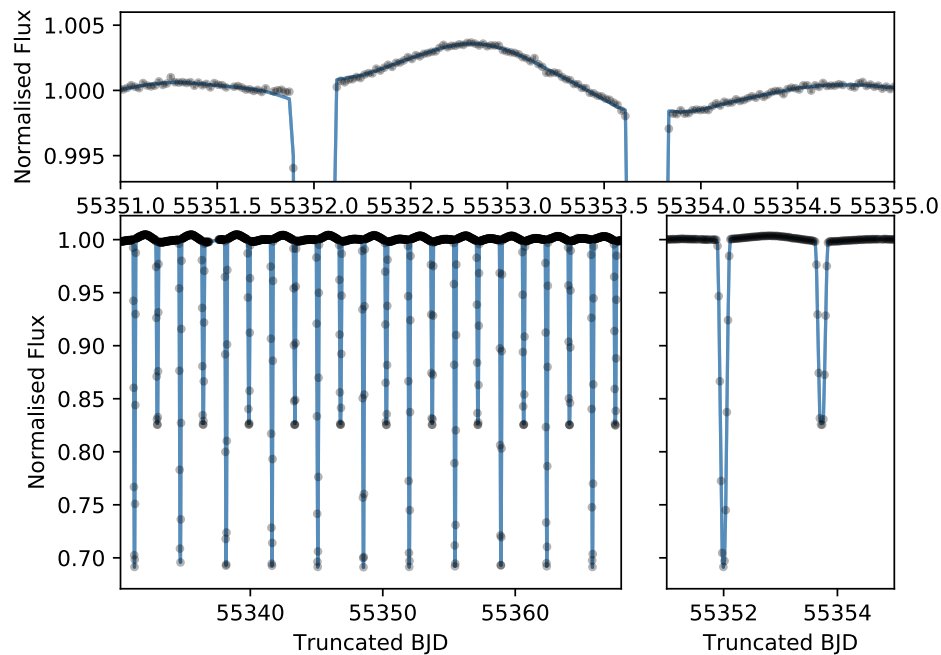


Figure 13. The *Kepler* light curve of KIC 5288543. Here the *Kepler* data are displayed as black points and the blue lines denote the PHOEBE binary star model and Gaussian processes combined. The out of eclipse variations are a combination of spots and ellipsoidal variations.

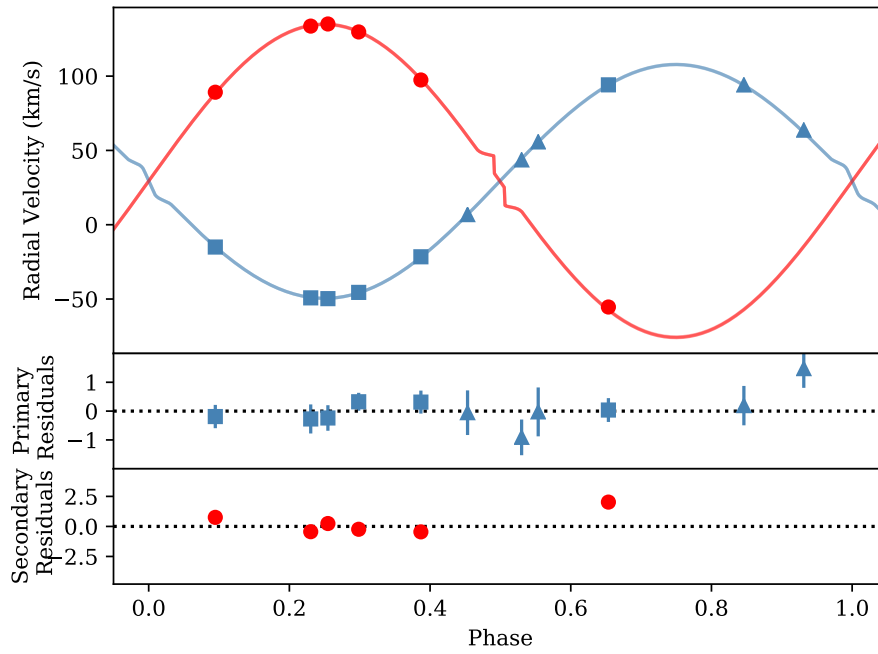


Figure 14. The figure depicts the APOGEE and HRS radial velocities, and PHOEBE model radial velocity curves for KIC 5288543. The format is the same as that of Figure 3.

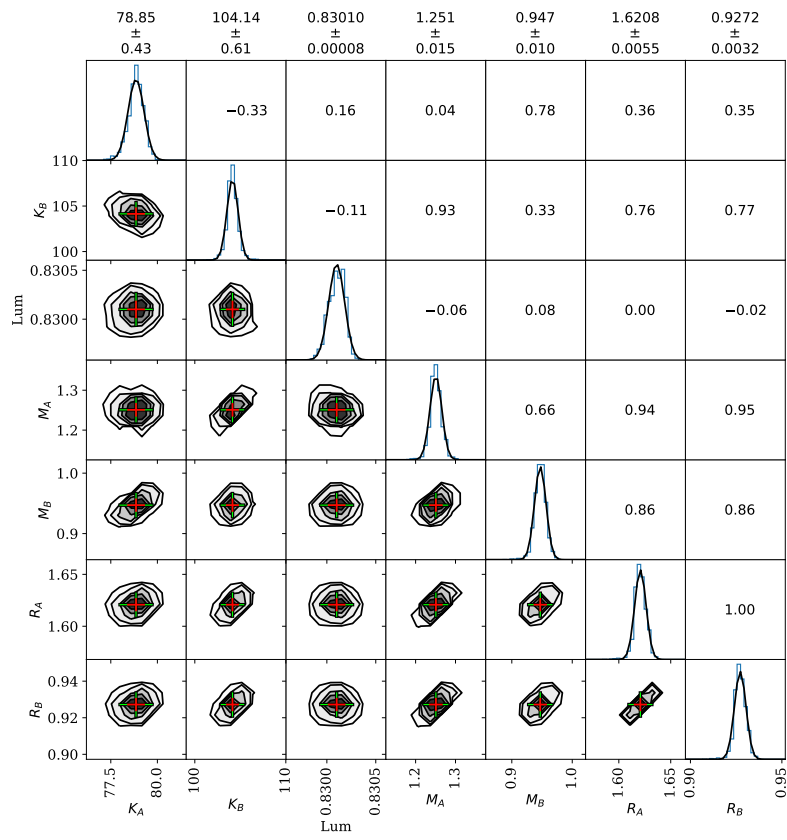


Figure 15. Distributions for KIC 5288543 where the figure has the same format as Figure 2.

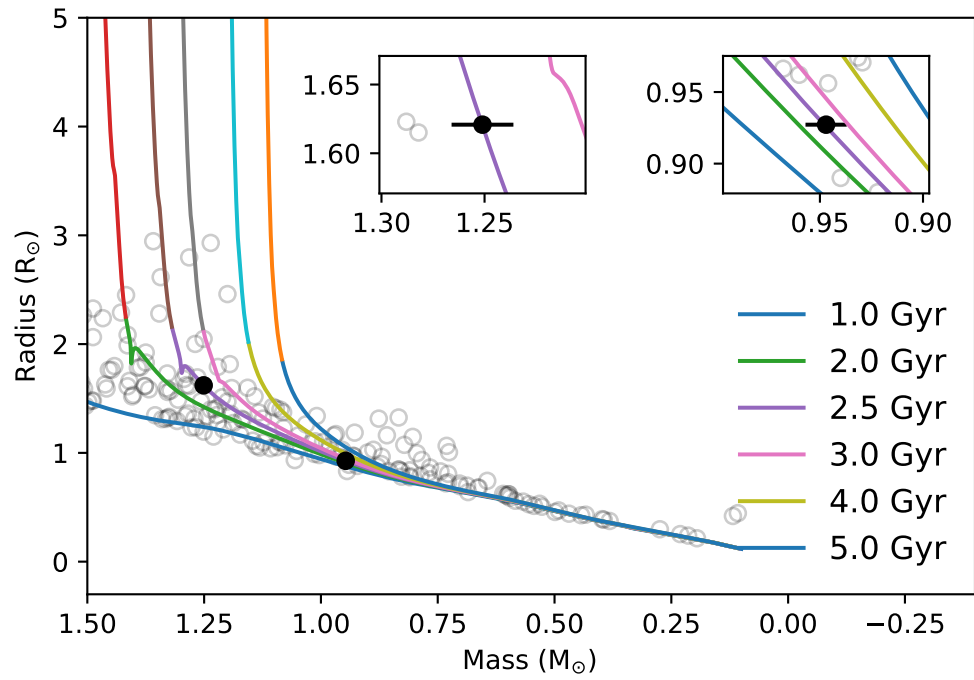


Figure 16. Radius vs mass for the components of KIC 5288543 where the figure is the same as Figure 4.